InAs/GaSb Type II superlattice barrier devices with a low dark current and a high quantum efficiency.

P.C. Klipstein, E. Avnon, Y. Benny, R. Fraenkel, A. Glozman, S. Grossman, O. Klin, L. Langoff, Y. Livneh*, I. Lukomsky, M. Nitzani, L. Shkedy, I. Shtrichman, N. Snapi, A. Tuito*, and E. Weiss

SemiConductor Devices P.O. Box 2250, Haifa 31021, Israel

* Israel MOD

ABSTRACT

InAs/GaSb Type II superlattices (T2SLs) are a promising III-V alternative to HgCdTe (MCT) for infrared Focal Plane Array (FPA) detectors. Over the past few years SCD has developed the modeling, growth, processing and characterization of high performance InAs/GaSb T2SL detector structures suitable for FPA fabrication. Our LWIR structures are based on an XB_pp design, analogous to the XB_nn design that lead to the recent launch of SCD's InAsSb HOT MWIR detector (T_{OP}= 150 K). The T2SL XB_pp structures have a cut-off wavelength between 9.0 and 10.0 μm and are diffusion limited with a dark current at 78K that is within one order of magnitude of the MCT Rule 07 value. We demonstrate 30 μm pitch 5 × 5 test arrays with 100% operability and with a dark current activation energy that closely matches the bandgap energy measured by photoluminescence at 10 K. From the dependence of the dark current and photocurrent on mesa size we are able to determine the lateral diffusion length and quantum efficiency (QE). The QE agrees very well with the value predicted by our recently developed $\mathbf{k \cdot p}$ model [Livneh et al, Phys. Rev. B86, 235311 (2012)]. The model includes a number of innovations that provide a faithful match between measured and predicted InAs/GaSb T2SL bandgaps from MWIR to LWIR, and which also allow us to treat other potential candidate systems such as the gallium free InAs/InAsSb T2SL. We will present a critical comparison of InAs/InAsSb vs. InAs/GaSb T2SLs for LWIR FPA applications.

1. INTRODUCTION

InAs/GaSb Type II superlattices (T2SLs) are a promising III-V alternative to HgCdTe (MCT) for infrared Focal Plane Array (FPA) detectors[1]. Recently it was proposed that gallium-free InAs/InAsSb T2SLs may offer superior performance due to their longer carrier lifetime[2]. Over the past few years SCD has developed the modeling, growth, processing and characterization of high performance InAs/GaSb T2SL detector structures suitable for FPA fabrication. These structures

have a cut-off wavelength between 9.0 and 10.0 μm and are based on a patented Long Wavelength Infra-Red (LWIR) pB$_p$$p$ design[3,4]

In a pB$_p$$p$ device, the dark current is diffusion limited, and there is no Generation-Recombination (G-R) contribution. This is in contrast to a p-n photodiode, where the G-R contribution is usually dominant. The suppression of the G-R current is achieved by ensuring that all three layers of the device (active, barrier and contact layers or AL, BL and CL) are doped p-type. This leads to a depletion electric field that is confined entirely within the wide bandgap BL when the device is at its operating bias. In a depleted semiconductor material, the G-R current is activated with an energy of half the bandgap, and since even half the bandgap of the BL is much larger than the whole bandgap of the AL, the G-R current is negligible in comparison with the diffusion current from the AL. Thus, the detector behaves electrically like a wide bandgap device, while optically it behaves like a narrow bandgap device. Minority carriers optically excited in the AL may diffuse freely across the BL and into the CL. The device has a photoconductive gain of one.

Figure 1
Schematic band profile of a pB$_p$$p$ device made from InAs/GaSb and InAs/AlSb T2SLs, at its operating bias.

Figure 1 shows the layer arrangement and band profile of a pB$_p$$p$ device, as described above, close to its operating bias. The AL and CL are both made from InAs/GaSb Type II superlattices (T2SLs) with approximately 13 monolayers (ML) of InAs and 7 ML of GaSb. The interfaces are InSb-like and their presence ensures a good lattice match with the GaSb substrate. Photons enter the device from the back-side of the AL, where they are able to excite minority carriers. The barrier layer is based on an InAs/AlSb T2SL design with approximately 15ML of InAs and 4 ML of AlSb. By careful adjustment of the precise InAs layer thicknesses in the two superlattices, it is possible to obtain a nearly smooth conduction band profile, with no significant discontinuities.

Over the past few years, we have developed a suite of simulation packages which can be used to calculate the spectral response of a pB$_p$$p$ device, and more generally, an XB$_p$$p$ device where a different contact material is used. The only input required is the bandgap and period of each of the superlattices, their stack thicknesses and refractive indices, the optical thickness of any antireflection coating, and also the minority carrier diffusion length and backside surface recombination velocity in cases where these latter two are small enough and large enough, respectively, to reduce the performance below its ideal value. We are also able to simulate the performance of polarity reversed XB$_n$n devices, for example where the AL is based on an InAs/InAsSb T2SL. In this case the BL is made from an AlSbAs alloy. No analogous XB$_p$$p$ structures exist for this AL material due to the lack of a suitable BL.

This paper is arranged as follows. In section 2, we describe our methods of device design and simulation of performance. In section 3, we present dark current measurements on some representative pB$_p$$p$ devices grown in our Veeco Gen III Molecular Beam Epitaxy (MBE) machine. We compare their dark current values with the values predicted by MCT Rule 07[5], which has become the Industry standard, for state of the art photodiodes made from MCT. In section 4 we present measurements of quantum efficiency (QE) as a function of AL thickness and show that the results agree quite well with our simulations. Finally, in section 5, we present the results of QE simulations for an InAs/InAsSb XB$_n$n device and compare them with those obtained for an InAs/GaSb XB$_p$$p$ device. In section 6, we present our conclusions.

2. METHODS OF DEVICE DESIGN AND PERFORMANCE SIMULATION

In order to exploit the full potential offered by bandgap engineering in antimonide superlattices, it is essential to develop good predictive software for the band energies, dispersions and densities of states of each superlattice. From these quantities it is possible to achieve the correct band alignments in barrier structures, such as the XB$_p$$p$ device, and to calculate the absolute value of the absorption coefficient for the AL as a function of photon wavelength. The absorption coefficient can be used, in turn, to calculate the full spectral response of an XB$_p$$p$ detector, using optical transfer matrix techniques.
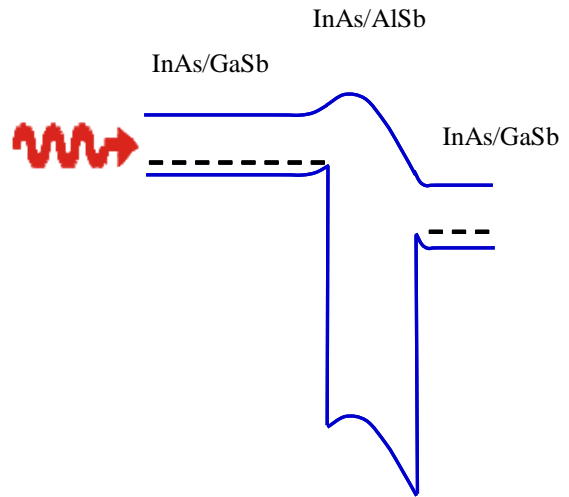
Our band structure simulations are based on a modified version of the $\mathbf{k} \cdot \mathbf{p}$ model for nearly lattice matched materials, which has a small number of input parameters[6]. This model was developed by one of the authors after Takhtamirov and Volkov [7] showed that the widely used Burt-Foreman approach is incomplete. Some notable points[8,9] in the model are:

(1) An interface matrix which is essentially diagonal in the case of no common atom (NCA) superlattices such as InAs/GaSb or InAs/AlSb, and which has three leading parameters: D_S, D_X and D_Z.

(2) An interface matrix which is essentially off-diagonal for common atom (CA) superlattices such as GaSb/AlSb or InAs/InAsSb, and which has two leading parameters, α and β.

(3) A reduction in the number of independent Luttinger parameters. Namely, using equation C1 of Ref. 8, four out of the six Luttinger parameters in any given superlattice (three for each material) can be expressed in terms of the other two, with no loss of precision. This means that in an $XB_p p$ structure based on InAs/GaSb and InAs/AlSb T2SLs, only two Luttinger parameters are required (e.g. γ_1 and γ_2 for InAs) instead of the usual nine. It also provides a direct way of determining all three parameters in the ternary layer of an InAs/InAsSb T2SL, which cannot be determined easily by any other method. It should be noted that standard methods of interpolation do not work for the alloy, due to strong bowing effects.

Figure 2 shows a comparison between the calculated bandgaps and the photoluminescence (PL) peak energies measured at 10K for a set of more than 30 InAs/GaSb T2SLs. The calculations were based on InAs and GaSb layer widths determined with a typical accuracy of ±0.2 ML, by finding a single pair of growth constants, which when multiplied by the beam fluxes and shutter timings gave the least RMS errors for the precisely measured superlattice periods[8]. The measured and calculated energies in Figure 2 match to within an accuracy of $\pm k_B T$ at 77K (thin dashed lines), for bandgap energies between 100 to 300meV (cut-off wavelengths between 4 and 12 µm). Figure 3 shows examples of measured (grey) and calculated (black) absorption spectra for MWIR and LWIR T2SL structures. All of the main features in the measured spectra are reproduced, including the strong peak due to zone boundary $HH_2 \rightarrow E_1$ transitions below 3 µm[8]. Our two independent Luttinger parameters are γ_1 and γ_2 for InAs, and they have fitted values of 19.77 and

(a)   (b)
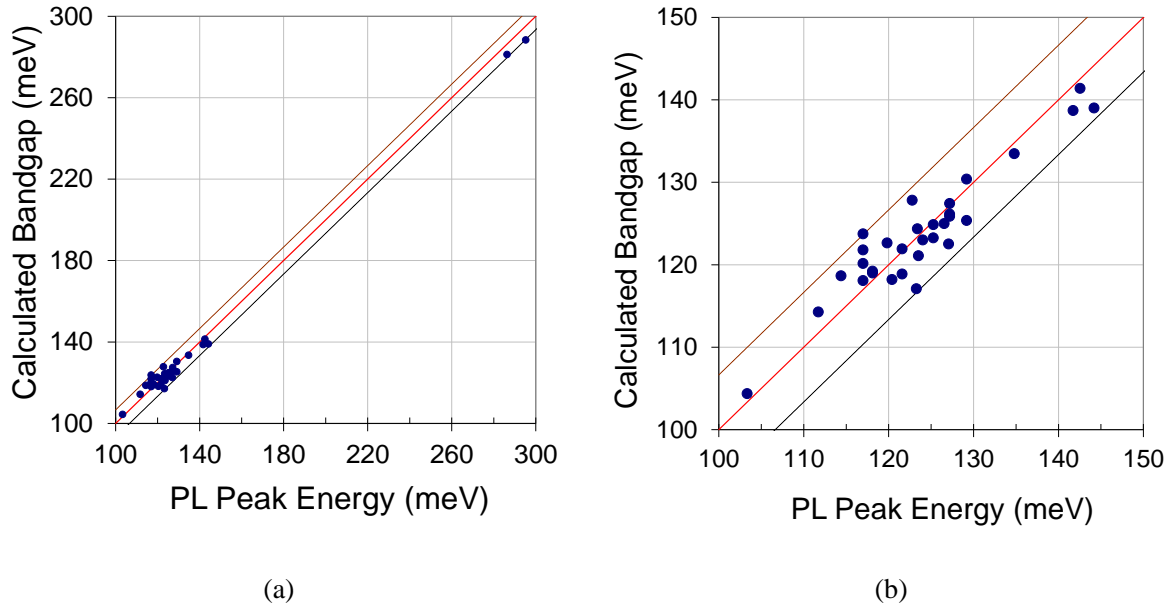
Figure 2
(a) Comparison between calculated bandgaps and PL peak energies measured at 10K for more than 30 InAs/GaSb T2SLs spanning the MWIR to LWIR wavelength range. Thin lines show deviation by $\pm k_B T$ at 77 K from ideal behavior (thick solid line) (b) Expanded view of the LWIR region.
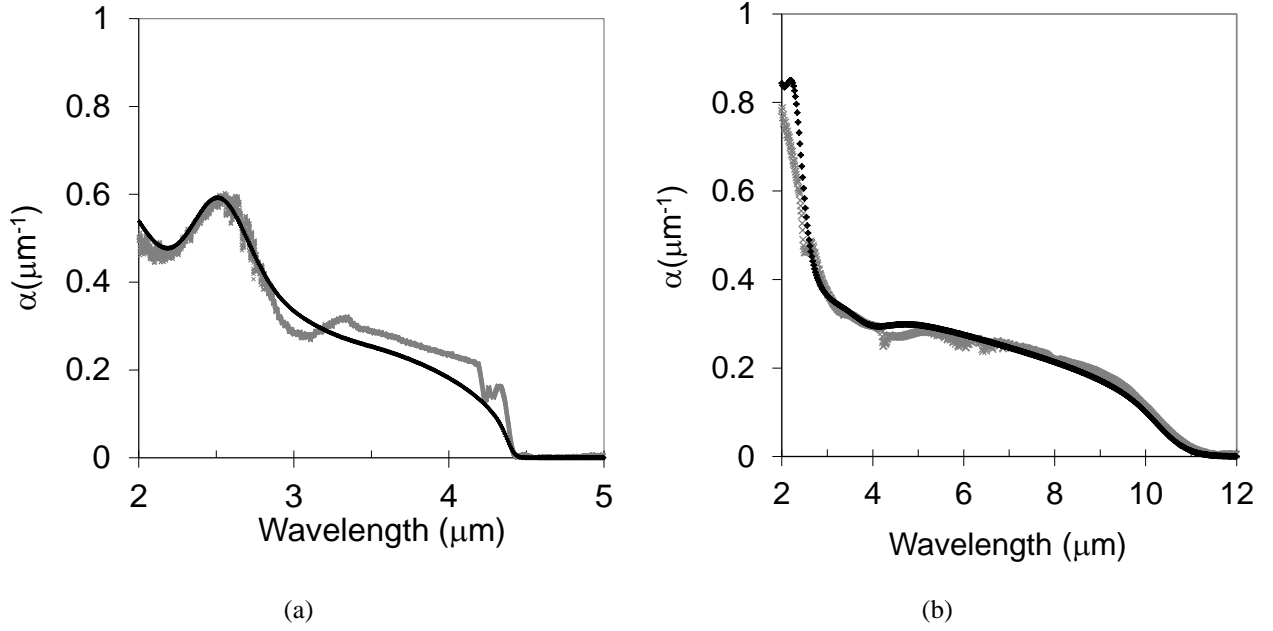
(a)

(b)

Figure 3
Measured (grey) and calculated (black) absorption spectra for (a) 8.4/13.7 MWIR and (b) 14.4/7.2 LWIR InAs/GaSb T2SLs (dimensions in ML). The large peaks at short wavelengths are from zone boundary $HH_2 \rightarrow E_1$ transitions

8.57 respectively. These values, and those of the four remaining Luttinger parameters calculated from them (γ_3 for InAs, and γ_1, γ_2, γ_3 for GaSb), are all within 3% of those proposed by Lawaetz[10]. The other parameters used in the calculation are the interface potentials: D_S, D_X, $D_Z = -1.70$, 1.17, -1.17 eV Å, and the Valence Band Offset: VBO $= -0.553$eV (with respect to the valence band of GaSb). The matrix element scaling parameter defined in Ref. 8 was $\eta=1.13 \pm 0.09$ [11]. It should be noted that if we omit the interface matrix, the calculated bandgaps in Figure 3 exhibit a blue-shift of about 0.75 μm for the MWIR T2SL and 4.5 μm for the LWIR T2SL. This demonstrates that the contribution of the interface potentials to the superlattice band structure is far from negligible.

We have also tested our model against experimental data on other InAs based superlattice structures, namely InAs/AlSb and InAs/InAsSb and it works remarkably well. In each case we use the same values of γ_1 and γ_2 for InAs (19.77 and 8.57) and do not need to introduce any other independent Luttinger parameters. Figure 4 shows a comparison between the measured and calculated bandgaps of fourteen InAs/AlSb superlattices. In this case, not all of the individual layer thicknesses could be determined to an accuracy of ±0.2 ML, and for these superlattices the resulting energy uncertainty is indicated with error bars. The largest thickness uncertainty was ±0.5 ML.

A comparison between the calculated and measured absorption spectrum for a 12.8 ML / 12.8 ML InAs/InAs$_{0.815}$Sb$_{0.185}$ T2SL is shown in Figure 5. Note that all the main features of the experimental spectrum in Figure 5 are reproduced by our calculation, including the bandgap, the strength of the
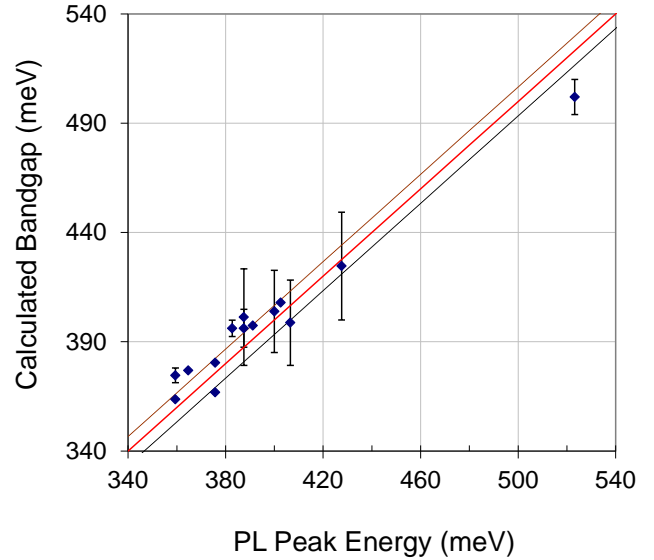

Figure 4
Comparison between calculated bandgaps and PL peak energies measured at 10 K for fourteen InAs/AlSb SLs.

absorption, and the wavelengths of the four points where the slope changes abruptly. Details of how the bandgaps and Luttinger parameters were determined for the $InAs_{1-x}Sb_x$ alloy are given in Ref. 12.

In order to simulate the spectral response curve of a superlattice barrier detector, we first calculate the absorption coefficient of the superlattice AL as described above and use it to determine the complex refractive index. We then use a combination of the optical transfer matrix technique[13,14] and the Van de Wiele model[15] to simulate the photoresponse. The model includes the surface recombination velocity on the back side of the AL and the minority carrier diffusion length. We also average over different thicknesses of the thin remaining transparent GaSb substrate in order to suppress Fabry Perot oscillations in the response curve. For simplicity we use the following values for the thickness (t) and the real part of the refractive index (n) in all cases (both $XB_p p$ and $XB_n n$) since any differences between refractive indices for the two structures are insignificant: t_{BL}=0.5 μm, t_{CL}=0.2 μm and n_{AL}=n_{CL}=3.6, n_{BL}=3.4. Some examples of calculated response spectra will be shown below, in
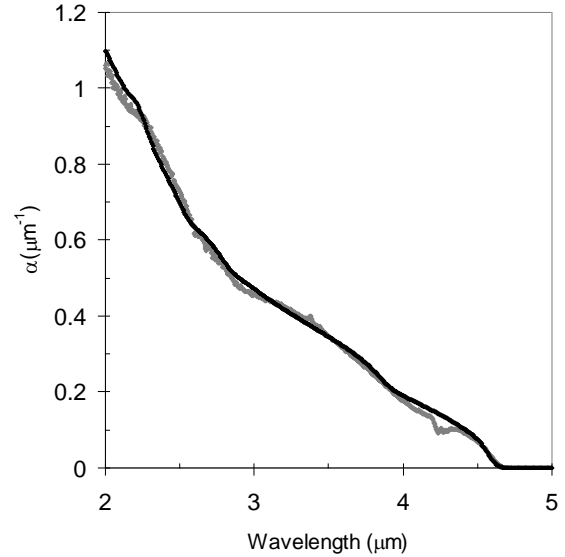

Figure 5
Comparison between calculated (black) and measured (grey) absorption spectra for a 12.8/12.8 $InAs/InAs_{0.815}Sb_{0.185}$ T2SL at 77 K

section 5, as a function of the minority carrier diffusion length, for a fixed AL thickness of 5 μm.

3. DARK CURRENT

In this section we present dark current measurements on some representative $pB_p p$ test devices made from wafers grown in our Molecular Beam Epitaxy (MBE) machine. Except where stated otherwise the AL thickness is 1.5 μm.

(a)

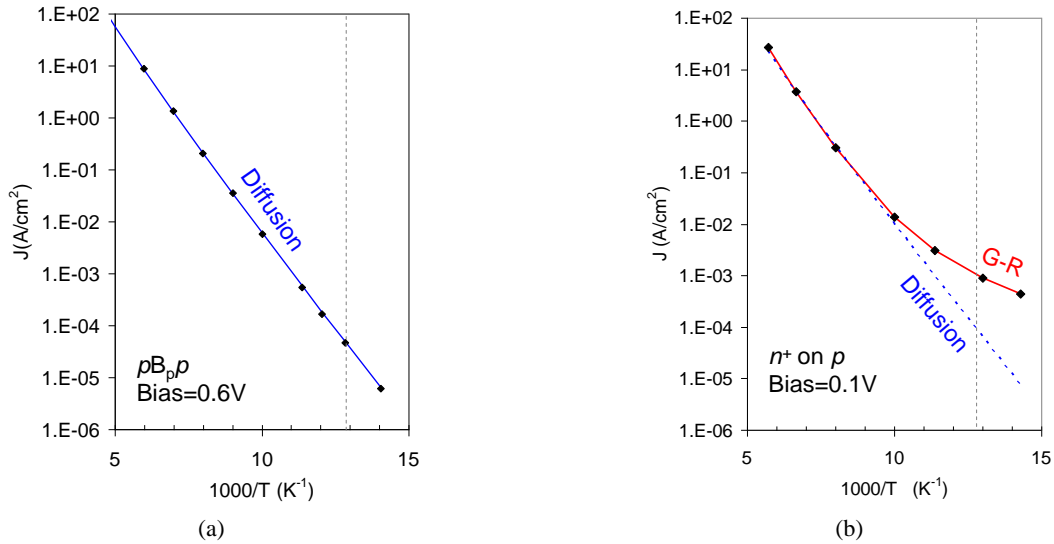(b)

Figure 6
Arrhenius plots of the dark current in InAs/GaSb 100×100 $μm^2$ mesa devices with a bandgap wavelength of ~10.0μm for (a) a $pB_p p$ structure at a bias of 0.6V and (b) a n+ on p diode structure at a bias of 0.1V. At 77K the diode exhibits a dark current that is more than one order of magnitude higher than that of the $pB_p p$ structure. The current in the $pB_p p$ structure is diffusion limited over the whole temperature range, while the diode is only diffusion limited above ~120K.

We start by comparing the dark current measured in a pB$_\mathrm{p}$$p$ device, with that in a n-on-p diode that has essentially the same p-type AL material. In Figure 6, Arrhenius plots of the dark current density at operating bias are shown for the two devices, each with a 100×100 μm^2 mesa: the pB$_\mathrm{p}$$p$ device in Figure 6(a) and the n-on-p diode in Figure 6(b). In each case the AL had a bandgap wavelength of ~10 μm (as determined by photoluminescence measurements at 10K) and the superlattice periods were essentially identical. For the pB$_\mathrm{p}$$p$ device, electrical isolation from neighbouring devices was achieved by etching the mesa through the CL to just below the upper surface of the BL, while for the diode the mesa was etched into the p-type AL. The vertical dashed line in each plot of Figure 6 denotes the ideal device operating temperature of 77K. It can be seen that at this temperature the dark current in the diode is more than one order of magnitude greater than that in the pB$_\mathrm{p}$$p$ device, and that this is due to the total suppression of the G-R current in the pB$_\mathrm{p}$$p$ device but not in the diode. The G-R current is activated with approximately half the
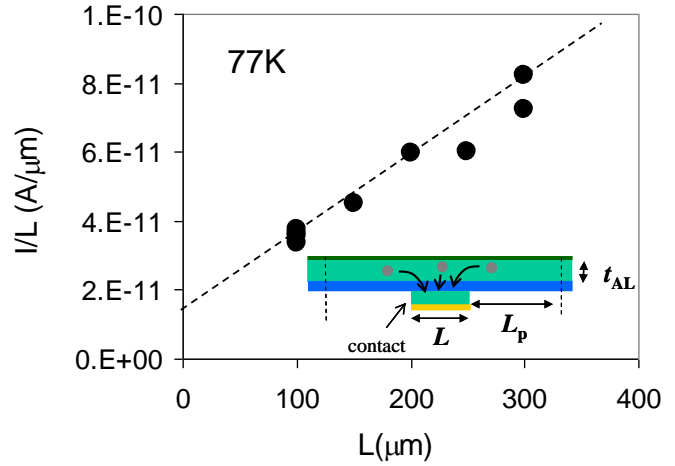

Figure 7
Plot of I_dark/L vs. L for variable size test devices made from an InAs/GaSb pB$_\mathrm{p}$$p$ structure with a bandgap wavelength of 9.7μm. The slope of the line through the points gives the bulk current density, J_B, while the y-intercept gives 4$\times$ the perimeter current density, J_P (Inset: contribution to perimeter current from lateral diffusion with diffusion length, L_p).
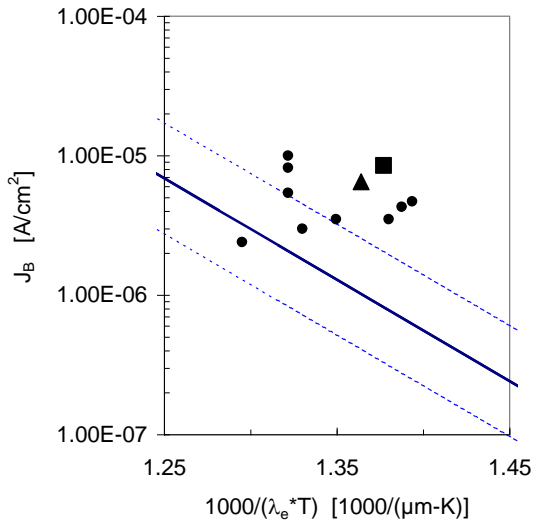
bandgap energy and, when present, this leads to a reduction in the slope of the Arrhenius plot at low temperatures, as is quite evident in Figure 6(b). On the other hand, the diffusion current is activated by the full bandgap energy and is the dominant dark current mechanism for the pB$_\mathrm{p}$$p$ device down to the lowest temperature shown of 71K. For the diode it is only evident above ~120K. Since the bandgaps are essentially the same, the diffusion lines shown in each figure are also very similar, in both slope and magnitude. They obey the formula: $J=J_0T^{2.5}\exp(hc/\lambda_\mathrm{A}k_\mathrm{B}T)$ with λ_A = 9.7 μm.

The temperature exponent of 2.5 is smaller than the value of 3 appropriate to bulk semiconductor devices because in a T2SL, the valence band is essentially two dimensional, while the conduction band is three dimensional.

The dark current in pB$_\mathrm{p}$$p$ test devices contains two components: a vertical diffusion component due to minority carrier

Figure 8
Rule 07 plot for InAs/GaSb pB$_\mathrm{p}$$p$ structures with an AL thickness of 1.5 μm (circle), 4.5 μm (triangle) and 6.0 μm (square), respectively. Range of bandgap wavelengths: $9.2 < \lambda_\mathrm{e} < 9.9$ μm. Solid line shows MCT Rule 07 with uncertainty factors of 2.5 (dashed lines)

transport towards the mesa along the growth direction, and a lateral diffusion component parallel to the BL, entering through the perimeter of the mesa area (see inset to Figure 7). This results in both a bulk and a perimeter contribution, according to the formula, $I_\mathrm{Dark} \approx J_\mathrm{B}L^2+4J_\mathrm{P}L$, where J_B and J_P are the bulk and perimeter current densities, and L is the side dimension of the
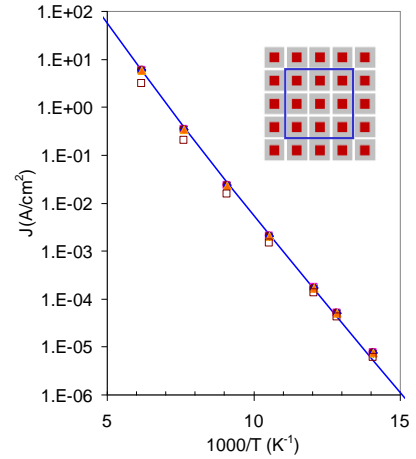
Figure 9
Arrhenius plot of current density for 25 InAs/GaSb pB$_\mathrm{p}$$p$ devices on a 5$\times$5 Fan-out array with a 30 μm pitch. The bandgap wavelength was ~9.6 μm. The open and closed points are explained in the text.

square mesa. In an ideal FPA, where the mesa size is close to the pixel size, and all pixels are biased with the same positive potential, the perimeter component should be negligible. Therefore the bulk component, J_B, is the key figure of merit of the T2SL material and device quality, and is the value expected for an ideal device of infinite area with no edge effects.

Figure 7 shows a plot of I_{Dark}/L vs. L, for eight pB$_p$$p$ test devices with mesa side dimensions of between 100 and 300 µm, in which the bandgap wavelength of the AL, measured by PL at 10K, was 9.7 µm. The dashed line is a linear fit whose slope yields a bulk current density of $J_B \sim 6.0 \times 10^{-6}$A cm^{-2}. In this way we have obtained 77K bulk current density values for more than ten pB$_p$$p$ structures, with bandgap wavelengths between 9.2 and 9.9 µm. The results are plotted in Figure 8, where they are compared with the MCT Rule 07 dark current (solid line) allowing a Rule 07 range of uncertainty of factor 2.5 (dashed lines)[5]. The circular, triangular and square points are for an AL thickness of 1.5, 4.5 and 6.0 µm, respectively. The results show that the dark currents for the InAs/GaSb T2SL structures are all within one order of magnitude of the Rule 07 values.

The Arrhenius plot of current density in Figure 9 shows results for 25 devices on a 5×5 Fan-Out (FO) array with a 30 µm pitch measured at the same operating bias of 0.95V, and it demonstrates the high uniformity and operability in our T2SL device material and process. The blue line through the points corresponds to a bandgap wavelength of λ_A=9.6 µm. The inset to the figure shows the layout of the array. The inner 3×3 matrix (within the blue square) has nine devices each individually connected by indium bumps to a lead on a silicon printed circuit board, while the outer 16 devices are all shorted to a single lead. The solid points in Figure 9 are for the individual devices and the open points are for the 16 outer devices, in each case normalized to the total device area. All 25 devices are operating and show virtually identical diffusion like behaviour, down to <77 K.

4. QUANTUM EFFICIENCY

We have measured the quantum efficiency of our pB$_p$$p$ devices on small FO arrays of two types. The FO-D array was described in the previous section and consists of a 5×5 array of 30 µm pitch devices, made to simulate a small region of an FPA. The FO-S array consists of variable area devices with square mesa sizes between 9×9 and 250×250 µm². In each case the devices are hybridized to a silicon printed circuit with indium bumps and all but the last few microns of the GaSb substrate is polished off, so that a negligible amount of light is absorbed by the GaSb. We did not apply an antireflection coating (ARC). In the FO-D array, the QE of a single device can be measured when the devices surrounding it are subjected to the same bias. This simulates the biasing arrangement of an FPA. Both types of FO array have a reflective top contact which reflects more than 90% of the light that impinges on it. In the FO-D array, the mirror fill-factor (FF) is 64%, i.e. the mirror occupies 64% of the total pixel area.

Figure 10 (a) shows a typical response curve for a 100×100 µm² pB$_p$$p$ device on a FO-S array with an AL thickness of 3µm. Figure 10 (b) shows a fit to the size dependence of the QE from all the devices on the array, according to the formula: $QE=QE_\infty(L+2L_p)^2/L^2$, where L_p is the lateral diffusion length. The fit is very good and yields values of QE_∞=36% and L_p= 2.3µm. Note that this small value for the lateral diffusion length may simply be the result of a short minority carrier

Figure 10
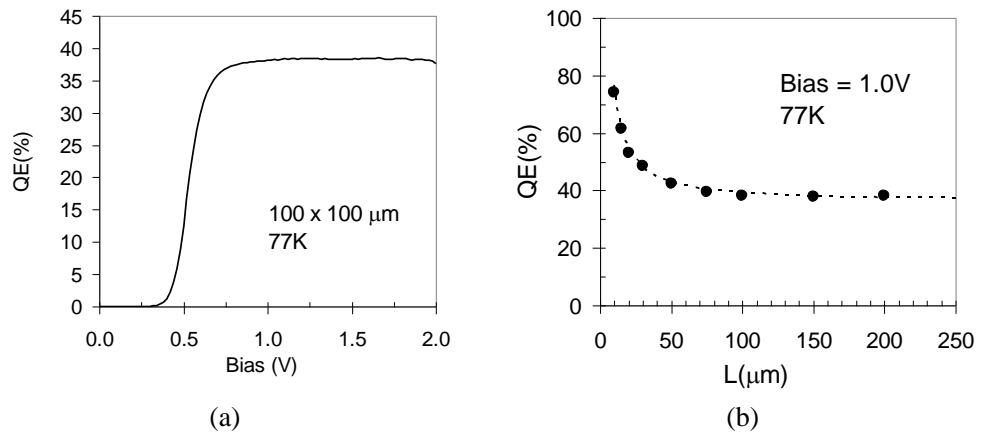(a) QE normalized to mesa area for InAs/GaSb pB$_p$$p$ device with t_{AL}=3µm, and L = 100 µm
(b) QE at bias = 1.0V vs. L (points) and fit to $QE_\infty(L+2L_p)^2/L^2$ with QE_∞=36% and L_p= 2.3µm (dashed line)

lifetime caused by recombination at the exposed surface surrounding the mesa of the device. The good agreement between the fitted value for the QE of 36% and the simulated value discussed below shows that there are negligible carrier losses in the bulk, and that the bulk diffusion length is significantly larger than the AL thickness of 3μm. This second conclusion is also supported by the constancy of the QE above the operating bias of 0.7V, showing no further increase, even when the AL starts to deplete.

The solid line in Figure 11 represents the QE simulated for a two pass FPA with a 64% mirror fill factor and no ARC, while the two points show the values measured for the FO-S array described above with an AL thicknesses of 3.0 μm, and for an FO-D array with an AL thicknesses of 1.5 μm, respectively. Note that for the FO-S array, the mirror FF is actually 100%, but since the AL is quite thick, the difference between simulated values with FF=64% and FF=100% is small.

For the simulations, the QE is determined from the total signal integrated over the Black Body (BB) spectrum at 23 C for a spectral window from 7.6μm to λ_G, where λ_G is the bandgap wavelength. For the measured values, the QE is the ratio of the measured number of electrons collected when the detector is placed in front of a BB at 23 C, and the calculated number of photons impinging on the detector over the same spectral window as above, since a filter is used in front of the detector which cuts off for $\lambda < 7.6$ μm. The bandgap wavelength is estimated from the PL at 10K. The agreement between experiment and simulation is quite reasonable.

The dashed line in Figure 11 shows the expected QE values when an ARC is used. Our simulations also show that to achieve a QE in excess of 60%, the AL thickness must be at least 4.5 μm.
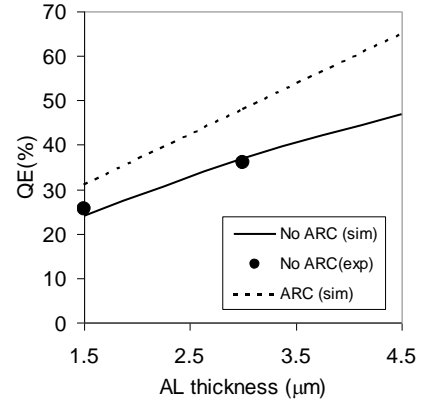

Figure 11
Simulated QE in two pass InAs/GaSb pB$_p$$p$ detectors with (dash) and without (solid line) an ARC, for AL thicknesses between 1.5 and 4.5 μm, and comparison with experimental measurements (points)

5. PERFORMANCE COMPARISON OF InAs/GaSb AND InAs/InAsSb LWIR BARRIER DETECTORS

InAs and As-rich InAsSb diodes are known to be very hard to passivate, due to a very strong accumulation layer that forms on exposed surfaces[16]. As for the InAs/GaSb T2SL devices discussed in this work, a more successful approach is to use a "barrier detector" architecture[3,4,17] which also leads to a lower dark current. Recently, InAs/InAsSb T2SLs have been proposed as a replacement for the lattice matched InAs$_{0.91}$Sb$_{0.09}$ alloy used in the AL of such XB$_n$$n$ detectors grown on GaSb[18]. The cut-off wavelength can then be extended beyond ~4.2 μm, which is the wavelength of the lattice matched alloy and which lies roughly in the middle of the MWIR atmospheric transmission window. Note that, as already mentioned in the Introduction, when an InAs/InAsSb T2SL is used, a suitable BL material (AlSbAs) only exists for the XB$_n$$n$ architecture[17]. In order to investigate the use of the InAs/InAsSb XB$_n$$n$ structure as an alternative to the InAs/GaSb LWIR pB$_p$$p$ devices considered in this work, we have compared simulated spectral response curves of InAs/GaSb and InAs/InAsSb barrier detectors with a 10 μm bandgap wavelength. Details of our simulation calculation were discussed above in section 2.

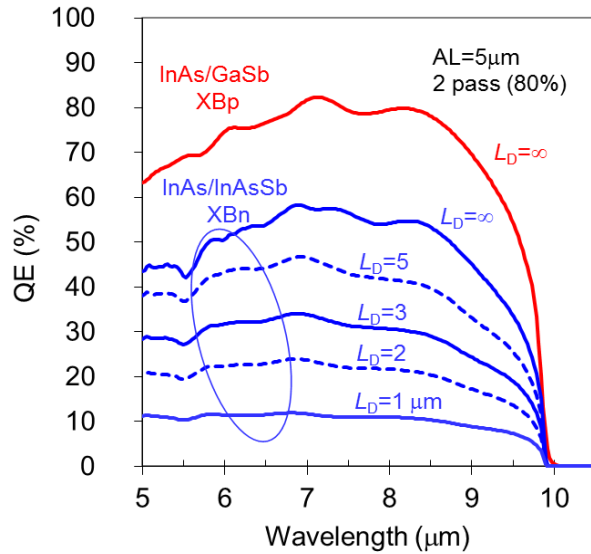For a reasonable Quantum Efficiency (QE) in a strain balanced InAs/InAsSb T2SL grown on GaSb, a

Figure 12
Calculated spectral response of a 13.8/7 InAs/GaSb XBp detector (red, solid) and a 31.5/9.5 InAs/InAs$_{1-x}$Sb$_x$ (x=0.39) XBn detector (blue, alternating solid and dash) at 77 K, as a function of the minority carrier diffusion length, L_D. In each case 80 % of the light is reflected back for a second pass, the ARC has an optical thickness of 2.17 μm, and the AL is 5 μm.

relatively high Sb concentration should be used, so that the T2SL period can be kept as small as possible. Figure 12 shows the calculated spectral response curves for two pass LWIR barrier detectors, each with a 5 μm AL thickness and with an antireflection coating of optical thickness, 2.17 μm. The two upper curves are for a 13.8/7 InAs/GaSb $XB_p p$ structure[9] and a 31.5/9.5 InAs/ $InAs_{0.61}Sb_{0.39}$ $XB_n n$ structure, respectively.

Since the dispersion of the valence mini-band is very narrow, the results for the $XB_n n$ case are shown as a function of the minority carrier diffusion length (L_D). Even when $L_D >> L_{AL}$, the QE of the $XB_n n$ detector is significantly below that of the $XB_p p$, due to the smaller absorption coefficient of the InAs/InAsSb T2SL. It is in fact much more likely that $L_D < L_{AL}$, since very small hole mobility values have been reported recently from direct measurements on n-type InAs/GaSb T2SL structures with a qualitatively similar valence band profile to the InAs/InAsSb T2SL considered here[19]. In Ref. 19 a vertical hole diffusion coefficient of 0.04 cm^2/s was reported at 77K for a 8/16 InAs/GaSb MWIR T2SL. For a typical minority carrier lifetime in such a MWIR T2SL of 65 ns [20], this corresponds to a hole diffusion length of only 0.5 μm. Moreover, when we calculate the valence band dispersion along the growth direction at zero and at small in-plane wave-vectors, for both the 8/16 InAs/GaSb T2SL of Ref. 19 and the InAs/InAsSb T2SL of Figure 12, the InAs/InAsSb T2SL exhibits the narrower dispersion. Therefore even though the InAs/InAsSb T2SL has a carrier lifetime typically about one order of magnitude greater than that in the InAs/GaSb T2SL[2], its narrower valence band dispersion will tend to compensate for any enhancement of the diffusion length due to the longer lifetime, so hole vertical transport is unlikely to be any more effective in the InAs/InAsSb T2SL than in the InAs/GaSb T2SL. For these reasons we expect an upper limit on the diffusion length in the InAs/InAsSb T2SL of about 1 μm. The simulations in Figure 12 thus suggest that the maximum QE of the InAs/InAsSb $XB_n n$ detector is not expected to exceed about 10%. Even though the dark current in the InAs/InAsSb $XB_n n$ detector is also expected to be very small due to a combination of the long carrier lifetime and the small diffusion length, the low QE will limit the value of such a detector in applications which require a high sensitivity or a high frame rate.

6. CONCLUSIONS

We have used a modified version of the $\mathbf{k} \cdot \mathbf{p}$ model to calculate the bandgaps and absorption spectra of three types of T2SL based on InAs, namely InAs/GaSb, InAs/AlSb and InAs/InAsSb. Important features of the model are different interface matrices for CA and NCA superlattices, and a reduction in the number of Luttinger parameters from the usual six to just two independent parameters.

The two independent InAs Luttinger parameters deduced for the InAs/GaSb T2SLs were used without adjustment in the two other superlattice structures (InAs/AlSb and InAs/InAsSb). Most significantly, this approach provides a reliable way of calculating the three Luttinger parameters for the $InAs_{1-x}Sb_x$ alloy used in InAs/InAsSb T2SLs, even though it exhibits very strong bandgap bowing. Good agreement between our model and the experimental bandgap wavelengths was demonstrated for both InAs/GaSb and InAs/AlSb superlattices over a wide range of wavelengths, and between calculated and measured absorption spectra for MWIR and LWIR InAs/GaSb T2SLs and a MWIR InAs/InAsSb T2SL.

Using our $\mathbf{k} \cdot \mathbf{p}$ model we have designed $pB_p p$ structures with a bandgap wavelength of between 9.0 and 10.0 μm, based on a InAs/GaSb AL and CL, and an InAs/AlSb BL. The InAs/AlSb T2SL has a bandgap wavelength of around 3.0 μm, and in each case its conduction band is closely aligned with that of the InAs/GaSb T2SL. We have grown a number of these structures by MBE and the dark current and QE have been measured as a function of temperature in variable area test devices and in Fan-outs, with both constant and variable device sizes. The bulk dark current of ten different devices was shown to be within one order of magnitude of MCT Rule 07, while the QE was shown to agree very well with simulations for two devices with a 1.5 and 3.0μm AL thickness, respectively. A 5×5 pixel, 30μm pitch, Fan-out array showed 25/25 operating devices, with good uniformity of the diffusion limited dark current.

Having demonstrated that our model is able to provide a reasonably faithful simulation of the experimental absorption spectra for both InAs/GaSb and InAs/InAsSb T2SLs, we have used the simulated absorption spectra to calculate the two pass spectral response of an InAs/GaSb $XB_p p$ detector and an InAs/InAsSb $XB_n n$ detector, each with an active layer thickness of 5 μm and a cut-off wavelength close to 10 μm. In the case of the InAs/InAsSb $XB_n n$ detector, the response was calculated as a function of the minority carrier diffusion length, since the diffusion length is expected to be smaller than the active layer thickness due to the absence of dispersion in the InAs/InAsSb valence band. Even for a very large diffusion length, the InAs/InAsSb T2SL has a significantly lower QE than the InAs/GaSb T2SL, due to its weaker absorption coefficient. When the short diffusion length is taken into account, the InAs/InAsSb $XB_n n$

detector exhibits a much smaller QE (<10%) than the InAs/GaSb XB_pp detector (~70%). This may limit the value of the InAs/InAsSb XB_nn detector in LWIR applications which require a high sensitivity or a high frame rate.

REFERENCES

[1] L. Bűrkle and F. Fuchs, Handbook of Infrared Detection Technologies (*Pub*. Elsevier; *Eds*. M. Henini and M. Razeghi) p159; ibid. M. Razeghi and H. Mohseni, p 191 (2002)

[2] E. H. Steenbergen, B. C. Connelly, G. D. Metcalfe, H. Shen, M. Wraback, D. Lubyshev, Y. Qiu, J. M. Fastenau, A. W. K. Liu, S. Elhamri, O. O. Cellek and Y.-H. Zhang., Appl. Phys. Lett. **99**, 251110 (2011)

[3] P.C. Klipstein (2003) *Depletionless Photodiode with Suppressed Dark Current…*, US Patent 7,795,640 (2 July 2003)

[4] P.C. Klipstein (2006) *Unipolar semiconductor photodetector with Suppressed Dark Current…*, US Patent 8,004,012 (6 April 2006)

[5] W.E. Tennant, Journ. Electron. Mater. **39**, 1030 (2010)

[6] P.C. Klipstein, Phys. Rev. B **81**, 235314 (2010)

[7] E.E. Takhtamirov and V.A. Volkov , JETP **89**, 1000 (1999)

[8] Y. Livneh, P.C. Klipstein, O. Klin, N. Snapi, S. Grossman, A. Glozman, and E. Weiss, Phys. Rev. B **86**, 235311 (2012)

[9] P.C. Klipstein, Y. Livneh, O. Klin, S. Grossman, N. Snapi, A. Glozman, and E. Weiss, IR Physics and Technology **59**, 53 (2013)

[10] P. Lawaetz, Phys. Rev. B**4**, 3460 (1971)

[11] The fits in Fig. 3 are better than reported previously due to the correction of a computational error (erratum to be published). The new set of fitting parameters given in this work are therefore different from those given previously (see Refs. 8 and 9). As previously we have also used $\alpha=\beta=0.2$ eV Å (in order to see a spin splitting in the in-plane dispersion due to α) but setting them to zero has almost no effect.

[12] P.C. Klipstein, Y. Livneh , A. Glozman, S. Grossman, O. Klin, N. Snapi, E. Weiss, *Proc. 2013 U.S. Workshop on the Physics and Chemistry of II-VI materials*, Journ. Electron. Mater., accepted for publication (2014)

[13] J. Lekner, Theory of Reflection, (Springer Verlag, Berlin, 1987)

[14] P.C. Klipstein, O. Klin, S. Grossman, N. Snapi, B. Yaakobovitz, M. Brumer, I. Lukomsky, D. Aronov, M. Yassen, B. Yofis, A. Glozman, T. Fishman, E. Berkowicz, O. Magen, I. Shtrichman, and E. Weiss*,* Proc. SPIE **7608**, 7608-1V (2010)

[15] F. Van de Wiele, Solid State Imaging (Pub. Noordhoff International) p44 (1976)

[16] R.A. Stradling in *"Growth and Characterisation of Semiconductors"* edited by R.A. Stradling and P.C Klipstein, pp 165-185 (Adam Hilger, Bristol and New York 1990)

[17] P.C. Klipstein, O. Klin, S. Grossman, N. Snapi, I. Lukomsky, M. Yassen, D. Aronov, E. Berkowicz, A. Glozman, O. Magen, I. Shtrichman, R. Fraenkel and E. Weiss, Proc. SPIE **8268**, 8268-0U (2012)

[18] H.S. Kim, O.O. Cellek, Zhi-Yuan Lin, Zhao-Yu He, Xin-Hao Zhao, Shi Liu, H. Li and Y.-H. Zhang, Appl. Phys. Lett. **101**, 161114 (2012)

[19] B.V. Olson, "*Time-resolved measurements of charge carrier dynamics and optical nonlinearities in narrow-bandgap semiconductors*" dissertation, University of Iowa.(http://ir.uiowa.edu/etd/2596), (2013)

[20] G. Belenky, G. Kipshidze, D. Donetsky, S. P. Svensson, W. L. Sarney, H. Hier, L. Shterengas, D. Wang, and Y. Lin, Proc. SPIE **8012**, 8012-0W (2011)